sustainability

MDPI

Article

Hydrodynamic Characteristics of Strong, Unsteady Open-Channel Flow

Keke Hu [1], Jian Hu [2], Tianwei Huang [3], Xiangwei Ye [4], Shu Jiang [5,*] and Ying-Tien Lin [3,6,7,*]

1 Zhejiang Institute of Hydraulics & Estuary (Zhejiang Institute of Marine Planning and Design), Hangzhou 310020, China
2 Wenzhou Communications Develop Group Co., Ltd., Wenzhou 325000, China; hujian3@163.com
3 Institute of Port, Coastal and Offshore Engineering, Ocean College, Zhejiang University, Zhoushan 316021, China
4 Qiantang River Basin Management Center of Zhejiang Province, Hangzhou 310000, China; et332211@126.com
5 School of Economics and Management, Zhejiang Ocean University, Zhoushan 316022, China
6 Engineering Research Center of Oceanic Sensing Technology and Equipment, Zhejiang University, Ministry of Education, Zhoushan 316021, China
7 Donghai Laboratory, Zhoushan 316021, China
* Correspondence: jiangshu@zju.edu.cn (S.J.); kevinlin@zju.edu.cn (Y.-T.L.)

Abstract: Due to climate change, the intensity of extreme rainfall has been observed to increase with a shorter duration, causing flash floods (strong, unsteady flow) that lead to serious loss of life and economic damage all over the world. In this study, by repeating the same flume experiments twenty times over a bare bed or with a submerged vane installed, the hydrodynamic characteristics of a strong, unsteady open-channel flow were investigated. Acoustic Doppler velocimetry (ADV) was used to measure the instantaneous three-dimensional velocity, and the ensemble average method was then adopted to obtain the time-varying mean flow velocities. Reynolds decomposition was applied to disintegrate the instantaneous velocity to time-varying average velocity and fluctuating velocity. Turbulence characteristics such as turbulent intensity, turbulent bursting, and power spectral density (PSD) were analyzed against water depth variations. The results show that the loop pattern of the streamwise velocity against the water depth variations could significantly affect the turbulence characteristics of unsteady flow. Near the bed, the peaks of the turbulent intensity and the TKE lag behind the peak of the water depth. The PSD revealed that the turbulent energy increases at the rising and falling stages were due to the generation of small-scale turbulence vortices or eddies. As a submerged vane was present, the increase in the angle of attack caused the increase in the turbulent intensity and TKE, which means that the induced vortex became stronger and the wake region was larger. When the angle of attack was equal to 20°, the TKE abruptly enlarged in the falling stages, implying the breaking-up of the induced vortex. The PSD of the transverse fluctuation velocity showed multiple spikes at the high-frequency part, possibly denoting the shedding frequency from the induced vortex. Further downstream, behind the submerged vane, the peak frequencies of the PSD became imperceptible, likely because of the induced vortex decays or other factors such as the turbulence generated from the free surface or the channel bed mixing with the turbulence from the induced vortex.

Keywords: strong unsteady flow; ensemble average method; acoustic Doppler velocimetry; submerged vane; turbulence characteristics; power spectral density

check for updates

Citation: Hu, K.; Hu, J.; Huang, T.; Ye, X.; Jiang, S.; Lin, Y.-T. Hydrodynamic Characteristics of Strong, Unsteady Open-Channel Flow. *Sustainability* **2023**, *15*, 12821. https://doi.org/10.3390/su151712821

Academic Editors: Mateusz Hämmerling, Tomasz Tymiński and Tomasz Kałuża

Received: 12 February 2023
Revised: 4 June 2023
Accepted: 6 June 2023
Published: 24 August 2023

Copyright: © 2023 by the authors. Licensee MDPI, Basel, Switzerland. This article is an open access article distributed under the terms and conditions of the Creative Commons Attribution (CC BY) license (https://creativecommons.org/licenses/by/4.0/).

1. Introduction

The unsteady flow of natural rivers often occurs during the flooding period. Recently, due to climate change, the intensity of extreme rainfall has been observed to increase with a shorter duration, causing flash floods—one of the most significant natural hazards—and leading to serious loss of life and economic damage all over the world [1–4]. It is extremely

important to understand hydrodynamic characteristics during such flash floods (also called strong unsteady flow). Previously, field and laboratory measurements [5,6] showed that the bed load transport processes during flooding are quite different from those during steady flow. In recent years, despite the availability of elaborate experimental equipment, studies on unsteady flow have still been rare due to the fact that instantaneous velocity is difficult to separate from the mean velocity and fluctuating velocity components. Using elaborate equipment, such as the laser Doppler anemometer (LDA) and acoustic Doppler velocimeter (ADV), several attempts to understand the unsteady open-channel flow were carried out in the past decade. Nezu et al. [7] used LDA to determine the unsteady flow velocity and applied the Fourier decomposition method to extract the mean time-varying velocity and turbulent velocity. The distributions of the mean velocity and turbulence characteristics across the river depth were compared with those during unsteady, closed, wall-bounded turbulent flows. According to their results, turbulent intensity was larger in the rising stage than that in the falling stage, except in the area very near the free surface. Furthermore, the unsteadiness of the open-channel flow could only affect the friction velocity but not the fluctuation velocity and Reynolds stresses. In terms of bed shear stress, it reached its peak before the discharge peak. This is helpful in explaining that sediment transport in an unsteady open channel is larger in the rising stage than in the falling stage. Song and Graf [8] used an acoustic Doppler velocity profiler (ADVP) to study the turbulence characteristics of an unsteady open channel over gravel beds. They obtained the horizontal and vertical turbulence intensities and the Reynolds shear stress in the rising stage, which are generally larger than those in the falling stage. Through field observations, Hopkinson [9] found that the near-boundary velocity during the rising stage is lower than that in the falling stage, likely due to the measurement location and local roughness. These studies provide valuable insights into the hydrodynamic characteristics of unsteady flow. However, turbulence features during flash floods, i.e., during strong unsteady flow, are given less attention and are still not well understood.

According to previous studies on unsteady open-channel flow, the most important aspect seems to be the determination of the mean velocity component. To circumvent this difficulty, there are principally five kinds of methods applied to determine the mean velocity from the measured velocity profile [7,10,11]: (1) The ensemble average method, (2) the moving time-average method, (3) the Fourier component method, (4) the wavelet method, and (5) the empirical mode decomposition (EMD) method. The ensemble average method can be performed provided that the experimental conditions can be repeated. The empirical mode decomposition method has recently been developed by Huang et al. [12], who used it extensively to analyze nonstationary and nonlinear time-series data for different geophysical applications [13]. Although the ensemble average method is the most reliable approach for extracting time-varying average flow quantities [14], due to the practical and technical limitations, time constraints, and limited resources [15], this method is seldom applied in studies on unsteady open-channel flow. For the other three methods, there is a weakness that likely causes errors in the estimation of the time-varying mean flow quantities. With regard to the moving time-average method, determining the size of the time-average window is challenging. For the Fourier component and wavelet methods, the cut-off frequency needs to be decided [16], and for the EMD method, the number of residual terms needed during the sifting process is still controversial [17].

In this study, we aim to understand hydrodynamic characteristics during a strong, unsteady open-channel flow, i.e., during flash floods. The ensemble average method, which is the most reliable approach for extracting time-varying mean flow quantities, was thus adopted. With the help of a feedback control circuit, repeated flume experiments under the same unsteady flow conditions were carried out so that the ensemble average method could be implemented. Once the time-varying average flow quantities during unsteady flow events had been obtained, the turbulent quantities were calculated using Reynolds decomposition. The experiments were divided into two parts: one involved unsteady open channels without any obstructions in the flume (bare bed), and the other served to

discuss the effect of unsteady flow when a submerged vane is installed in the channel, oriented at an angle to the local velocity, and immersed in water. Submerged vanes were used to stabilize and modify channel morphology and alignment [18]. Many studies have proven the effectiveness of submerged vanes in channel meander realignment [19], bank stabilization [20], bed adjustment for navigational purposes, and so on [21,22]. Our main focus is on the turbulence characteristics of the vortex shedding from the trailing edge of the vane during the unsteady flow periods. This paper is organized as follows: In Section 2, we provide a detailed description of the experimental set-up and the number of times the experiments were repeated in ensemble-average realizations. In Section 3, we report and discuss the experimental results, including time-varying flow velocities and turbulence characteristics such as turbulent intensity, power spectrum, and bursting events with different unsteady flow conditions and vertical locations. Finally, a conclusion and future prospects are given in Section 4.

2. Materials and Methods

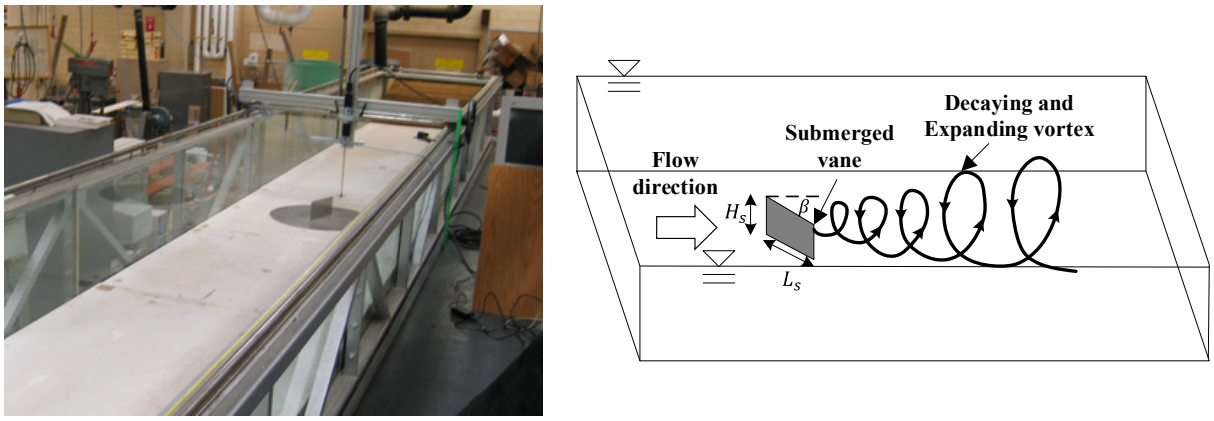
2.1. Experimental Apparatus

Experiments were carried out in a 12.19 m long and 1.22 m wide slope-adjustable (by lifting or lowering the upstream flume elevation), recirculating, and smooth flume in the Laboratory of Environmental Fluid Mechanics of the University of Wisconsin–Madison, USA. Water flow rate was adjusted through a butterfly valve located immediately upstream of a tee. A flowmeter, upstream of the butterfly valve, continuously measured the discharge coming through the system. The valve, which was controlled by a feedback control circuit, was able to make the flow condition repeatable.

The instrument used to measure the three-dimensional instantaneous velocities in this study was a Sontek 10 Mhz Acoustic Doppler Velocimeter (ADV), where x is longitudinal direction, y is transverse direction, and z is vertical direction, i.e., longitudinal velocity (u), transverse velocity (v), and vertical velocity (w). The semi-intrusive instrument is superior to other more intrusive methods. The ADV's probe was situated approximately 5 cm above the location of the actual sample volume (where measurements were taken). The ADV determines water velocities based on the Doppler shift principle. Details of the ADV's principle can be found in Sontek [23]. The ADV sampling volume used was 0.09 cm^3, with a sampling frequency of 25 Hz. The noise in the velocity measurements (=0.4 cm/s) was determined in still water. The water depth was recorded by using a camcorder with a video size of 640 $\times$ 480 $pixels^2$ and a sampling rate of 29.97 fps (frames per second). The resolution of the video was 0.0476 cm/pixel, which was good enough to obtain the variations in water depth. By converting the color image into a binary image, the water surface could be identified. The camcorder and the ADV were triggered simultaneously to ensure that the water depth data matched the ADV data.

2.2. Experimental Cases and Parameters

In this study, besides the bare-bed, unsteady flow cases, the unsteady flow conditions in the presence of a single submerged vane with different angles of attack β were tested. Figure 1 shows the picture of the experimental flume with a submerged vane and the schematic of a submerged vane and the induced vortex.



(**a**) (**b**)

Figure 1. (**a**) The experimental flume with a submerged vane, and (**b**) the schematic of a submerged vane and induced vortex.

An unsteadiness parameter α, proposed by Nezu et al. [7], is defined below:

$$\alpha \equiv \frac{1}{U_c}\frac{\partial h}{\partial t} \cong \frac{1}{U_c}\frac{h_p - h_b}{T_d} \tag{1}$$

where U_c = the convection velocity of turbulent eddies, approximately equal to $\frac{U_b+U_p}{2}$; U_b and U_p are the mean velocities at base flow and peak flow, respectively; h_b and h_p are water depth at base flow and peak flow; and T_d is the duration from the base discharge to the peak discharge. Nezu [24] mentioned that, if $\alpha = 0.0005$, the flow is weak and unsteady, and that the effects of unsteadiness are insignificant. In order to determine the flow conditions in the experiments, the Reynolds numbers Re and Froude numbers Fr were, respectively, calculated as follows:

$$Re = 4UR_h/v \tag{2}$$

and

$$Fr = U/\sqrt{gh} \tag{3}$$

where $R_h[= Bh_b/(2h_b + B)]$ is the hydraulic radius; B (=1.22 m) is the channel width; v = 10^{-6} m^2 s^{-1} is the kinematic viscosity of water; and g = 9.81 m^2 s^{-1} is the gravitational acceleration. Two unsteady flow conditions (UQ1 and UQ2) were used for the cases without a submerged vane; the flow conditions and relevant parameters are provided in Table 1. In the two cases, the base flow Q_b was maintained at the same level, and a peak flow Q_p ensuring that the back water would not overflow into the flume was chosen. As Nezu [24] mentioned, a flood flow with a U_c = 2 m/s and a rather large variation from h_b = 1 m to h_p = 5 m within T_d = 1 h would yield α = 0.00056. Considering a flash flood, the T_d would decrease and h_p would increase, and then α could go from $O(0.01)$ to $O(0.001)$, which would indicate that the flow is strong and unsteady [24], with O denoting the order of magnitude. In this study, the chosen α value was $O(0.01)$. Although this kind of flow represents very extreme conditions, it can offer a good chance to understand the response of hydrodynamics and turbulence to such strong unsteady flows.

The unsteady flow condition UQ2 was adopted for the cases with a submerged vane (the length L_v, height H_v, and thickness T_v of the vane were 0.32 m, 0.09 m, and 0.00159 m, respectively), and the ADV measurements were implemented behind the submerged vane at a constant height of h_m (9.08 cm from the channel bed). The fundamental variables are provided in Table 2.

Table 1. Flow conditions and experimental parameters without a submerged vane.

Case	Run	h_m (cm)	Duration T_d (Sec)	Base Flow Q_b (L/s)	Peak Flow Q_p (L/s)	h_b (cm)	h_p (cm)	Re_p	Fr_p	S	α
UQ1D1	30	0.77	4	42.08	87.70	18.42	19.88	217,620	0.260	0.006	0.0136
UQ1D2	20	6.98	4	42.08	87.70	18.42	19.88	217,620	0.260	0.006	0.0136
UQ2D1	20	0.43	4	42.08	83.59	21.75	23.96	196,775	0.187	0.007	0.0249
UQ2D2	20	9.08	4	42.08	83.59	21.75	23.96	196,775	0.187	0.007	0.0249
UQ2D3	20	11.58	4	42.08	83.59	21.75	23.96	196,775	0.187	0.007	0.0249

Note: For case code names, U, Q, and D denote unsteady, discharge, and depth, respectively. h_m is the height of velocity measurements; T_d is the duration from the base discharge to the peak discharge; h_b is the water depth at base flow; h_p is the water depth at peak flow; Re_p is the Reynolds number at peak flow; Fr_p is the Froude number at peak flow; S is the bed slope measured by a theodolite.

Table 2. Flow conditions and experimental parameters with a submerged vane (the flow condition is the same as that of UQ2D2).

Case	Run	h_m (cm)	Angle of Attack β	Measurement Location x_v/L_v
SQ2C0X03(UQ2D2SA0X03)	20	9.08	0	0.3
SQ2C10X03(UQ2D2SA10X03)	20	9.08	10	0.3
SQ2C10X4(UQ2D2SA10X4)	20	9.08	10	4
SQ2C20X03(UQ2D2SA20X03)	20	9.08	20	0.3
SQ2C20X4(UQ2D2SA20X4)	20	9.08	20	4

Note: For case code names, S, A, and X represent the submerged vane, angle of attack, and longitudinal distance behind the vane, respectively. x_v is the streamwise distance behind the submerged vane.

Figure 2 provides one experimental run for the time-varying water depth h and streamwise velocity of Cases UQ1D1 and UQ1D2 as an example. The streamwise velocity increased with the increasing water depth. Due to the back water effect (the water depth slowly increases), the data after 23 s have been removed and are excluded in subsequent analyses. According to water depth and streamwise velocity, the flow development can be divided as three stages: steady, rising, and falling stages. A time interval between the steady and rising stages was manually decided to avoid the mixture of steady and unsteady data. The time interval for the rising stage is defined as T_d, which will be used later to scale the time t for the unsteady flow event.

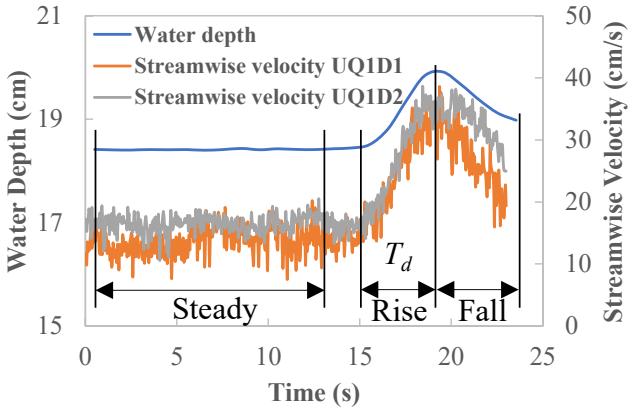


Figure 2. Time-varying water depth and instantaneous streamwise velocity for one run of Cases UQ1D1 and UQ2D2.

2.3. Ensemble-Averaging Processes and Reynolds Decomposition

In this study, the ensemble-averaging method was adopted to determine the time-varying mean flow velocities. The use of ensemble-averaging processes means that the

unsteady flow experiments with identical conditions were repeated N times. The time-varying mean flow velocity $\langle u_i \rangle$ can be determined as shown below:

$$\langle u_i \rangle = \frac{1}{N} \sum_{j=1}^{N} u_i^{(j)} \tag{4}$$

where the symbol $\langle\ \rangle$ represents the ensemble average, $u_i^{(j)}$ is the i-component instantaneous velocity obtained from the j-th experiment, and N is the total number of repeated experiments. Once the mean flow velocities are determined, the Reynolds decomposition can be applied to separate the mean quantity and the turbulent fluctuations from the instantaneous velocity, as given by the following equation:

$$u_i = \langle u_i \rangle + u_i' \tag{5}$$

where ' denotes the turbulent fluctuations. In this study, three-dimensional instantaneous velocities were measured, i.e., $i = 3$, $u_1 = u$, $u_2 = v$, and $u_3 = w$.

To implement the ensemble average method, it is important to check the effect of a different number of repetitions N on the ensemble-averaging process. Here, *TKE* (Turbulence Kinetic Energy), the mean kinetic energy per unit mass associated with eddies in turbulent flow, is defined by the following equation:

$$TKE = \frac{1}{2} \langle u'u' + v'v' + w'w' \rangle \tag{6}$$

where u', v', and w' are, respectively, x, y, and z three-dimensional fluctuating velocity, calculated using Equation (5). Figure 3 presents the *TKE* variations against the N values, which varies from 5 to 30 at five different times for Case UQ1D1. It was found that the *TKE* has slight variations if $N > 17$, close to the results in the study by Chang and Liu [25]. Although Chanson [15] and Chang and Liu [25] indicated that larger N values lead to lower uncertainty, performing a large number of repeated experiments is very time-consuming. Therefore, the N values, i.e., the number of repetitions, were set at 20 for the ensemble-averaging process in this study.

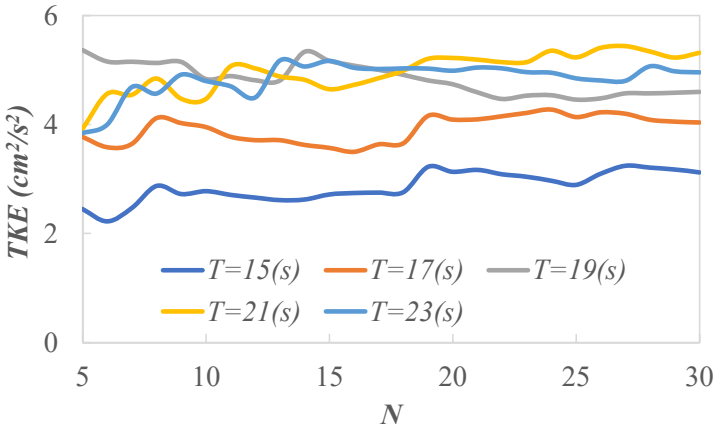


Figure 3. *TKE* against the number of repetitions N at different times for Case UQ1D1.

Figure 4 provides instantaneous and ensemble-averaged ($N = 20$) streamwise velocity values for Case UQ1D1. The red line can well represent the time-varying trend of the streamwise velocity of the unsteady flow.

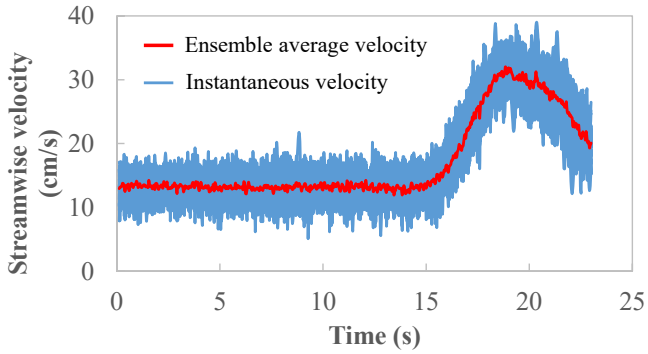


Figure 4. Instantaneous and ensemble-averaged streamwise velocity for Case UQ1D1.

2.4. Power Spectral Density

The turbulence spectrum performs the occurrence possibility F (f) (i.e., the spectral density) of turbulent eddies with different frequencies f at a fixed point. The high-frequency part represents the small-scale turbulence vortex, and the low-frequency part denotes the large-scale turbulence vortex in the turbulence spectrum [26]. The structure of the turbulence vortex and the transport and dissipation of *TKE* can be understood through spectral analysis [27]. In this study, the power spectral density (PSD) was analyzed based on the Welch method with the use of Hamming-type windowing [27], and it was implemented using the commercial software MATLAB by MathWorks.

3. Results and Discussions

3.1. Bare Bed Case

This section reports and discusses the experimental results of unsteady flows over a smooth and bare bed.

3.1.1. Time-Varying Water Depth and Streamwise Velocity

Figure 5 shows the ensembled loop property (hysteretic effect) of streamwise velocity against the water depth variations for bare bed cases, where $\Delta h = h - h_b$ and $\Delta h_p = h_p - h_b$. The streamwise velocity measured closest to the water surface was adopted, i.e., Cases UQ1D2 and UQ2D3. The loop properties of the two cases show considerable differences: one contains several crossings between the rising and falling stages (UQ1D1), and the other one is without any crossing. The traditional loop properties are the single loop or "eight-shape loop" [7]. The several-crossing loop pattern possibly indicates complicated unsteady flow patterns. The unsteadiness parameter α only performs the bulk property of unsteady flow, and the loop pattern could be used as another important factor to examine flow unsteadiness.

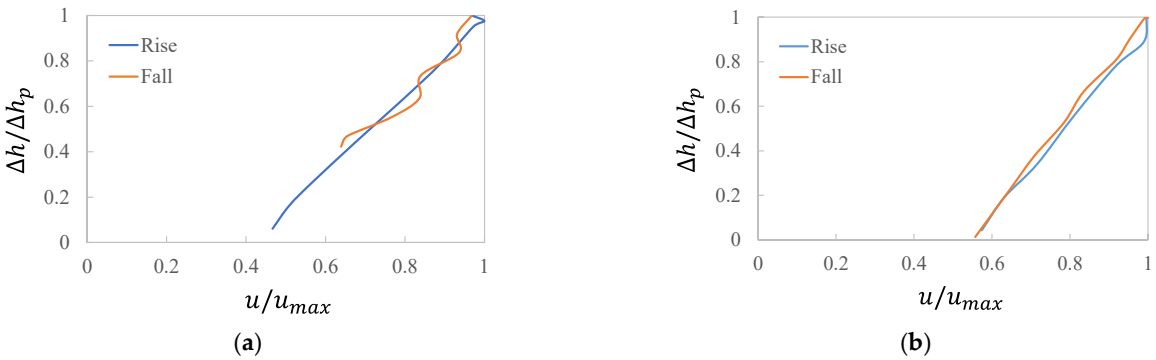


Figure 5. Loop property of streamwise velocity against water depth variations. (**a**) Case UQ1D2; (**b**) Case UQ2D3.

The time-varying water depth and streamwise velocity of the Cases UQ1 and UQ2 series at different water depths are presented in Figure 6. As previous studies [7,8] have mentioned, the maximum streamwise velocity occurs before the water depth reaches its peak. In addition, it was found that, for Case UQ1, the difference between the streamwise velocity near the bed and that away from the bed keeps increasing during the rising and falling stages of the unsteady flow. For Case UQ2, the differences between the streamwise velocity near the bed and away from the bed follows the trend of the water depth, and the velocity difference is larger in the falling stage than that in the rising stage. Furthermore, for Case UQ1, the peak of streamwise velocity occurs approximately at the peak of the water depth, but for Case UQ2, the streamwise velocity reaches the peak earlier than that of the water depth.

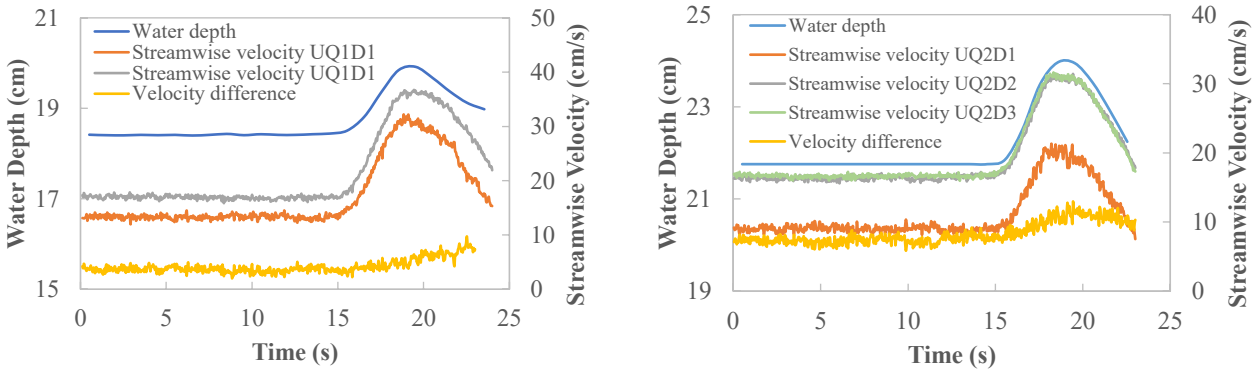


Figure 6. Time-varying water depth and averaged streamwise velocity. (**a**) Case UQ1 series; (**b**) Case UQ2 series.

3.1.2. Time-Varying Turbulent Intensity and Turbulence Kinetic Energy

Figure 7 shows the turbulent intensity (also called root-mean-square (rms) velocity) u_{rms}, v_{rms}, and w_{rms} against the water depth, where $u_{rms} = \sqrt{\overline{u'(t)^2}}$, $v_{rms} = \sqrt{\overline{v'(t)^2}}$, and $w_{rms} = \sqrt{\overline{w'(t)^2}}$, while "" is the average from twenty repeated runs. The values shown in Figure 7 were averaged over 1 s. It can be seen in Figure 7 that u_{rms}, is larger than those (v_{rms}, and w_{rms},) in the other two directions. Interestingly, v_{rms} is greater than w_{rms}. The possible cause is that the flume is very wide in comparison to the water depth, which produces a secondary circulation along the transverse direction. In addition, the turbulent intensity is larger near the bottom and becomes smaller when the measurement location is further away from the bottom, which is consistent with previous studies [7,8]. During the unsteady flow period, for Case UQ1D1 (closest to the bed), the peaks u_{rms}, v_{rms}, and w_{rms} apparently lag behind the peak of the water depth. For Cases UQ1D2 and UQ2D3, the peaks u_{rms}, v_{rms}, and w_{rms} generally appear before the water depth reaches its peak, which is similar to previous studies [7,8] regarding unsteady flows. For Case UQ2D1, the peaks of turbulent intensities u_{rms}, v_{rms}, and w_{rms} only slightly lag behind the peak of the water depth. However, for Cases UQ2D2 and UQ2D3, the peaks u_{rms}, v_{rms}, and w_{rms} appear before the water depth reaches its peak.

It is important to understand the TKE variations with the water depth, and—due to the absence of the streamwise velocity profile—the TKE values can be used as a surrogate to estimate bottom shear stress. To clearly demonstrate the trend of the TKE with the water depth, the dimensionless TKE values were obtained by scaling with the largest TKE (the measurement closest to the bed) at three measurement heights, and the water depth was non-dimensionalized by the peak water depth, as shown in Figure 8. Near the bed, the peak of the TKE appears after the water depth climaxes. In particular, for Case UQ1D1, it is apparent that the peak of the TKE lags behind the peak of the water depth. On the other hand, for Case UQ2D1, the peak of the TKE is only slightly behind the peak of the water

depth. For Cases UQ1D1 and UQ2D1 (closest to the bed), the phenomenon of a delayed TKE peak are contrary to the results of [5,6]. This could be due to the following reasons: (1) The flow condition is strong and unsteady, and the turbulence development near the bottom could be delayed due to the effect of bed friction; (2) the difference in streamwise velocity keeps increasing during the time-varying period, which could enlarge the TKE at the falling stage; and (3) the loop property, as shown in Figure 5a, is very complicated, which could change the turbulence activities in unsteady flows.

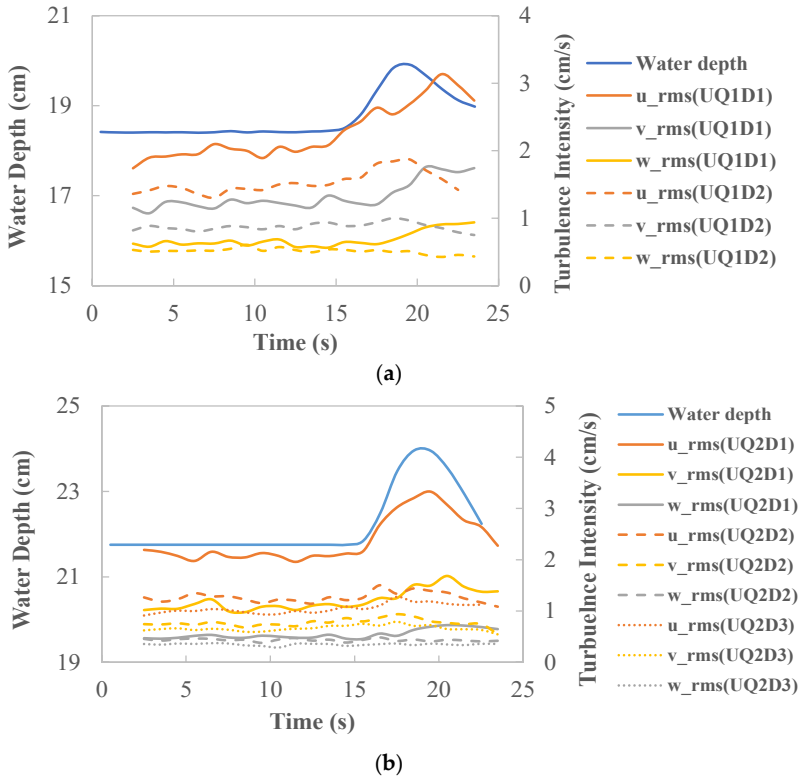


Figure 7. Time-varying turbulent intensities u_{rms}, v_{rms}, and w_{rms} against water depth. (**a**) Case UQ1 series; (**b**) Case UQ2 series.

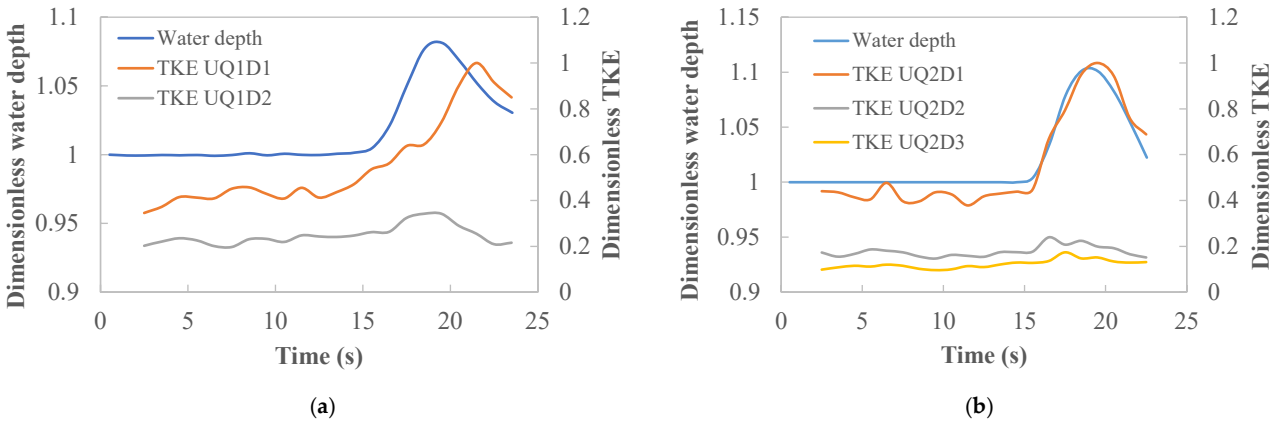


Figure 8. Time-varying dimensionless TKE against dimensionless water depth. (**a**) Case UQ1 series; (**b**) Case UQ2 series.

The near-bed TKE can be linked to the bottom shear stress τ_{bed} by using the following formula [26]:

$$\tau_{bed} \approx 0.2 \times TKE \quad (7)$$

Based on the TKE results, it can be estimated that the τ_{bed} is increased by 2.5 times during the unsteady flow period, which is larger than the increase of 1.5–2 times in the near-bed streamwise velocity (Figure 6b).

3.1.3. Turbulent Bursting

Fluid motions near the channel bed follow a clear "sequence of ordered motion (coherent motions)" [28]. For the quantification of the intermittent instantaneous Reynolds stresses as well as the identification of turbulence structures within a turbulent bursting sequence, one widely used conditional sampling technique is the quadrant analysis of the Reynolds shear stress [29,30]. In this study, quadrant analysis was conducted to study the effect of unsteady flow on turbulent bursting. In quadrant analysis, the Reynolds stress has four types of contributions according to the signs of the instantaneous velocity fluctuations [31], as expressed below:

(1) Quadrant I (outward interactions) $u' > 0$, $w' > 0$: a weak outward interaction of fluid away from the boundary (high-speed fluid reflected by the wall);
(2) Quadrant II (ejections) $u' < 0$, $w' > 0$: an ejection of low-speed fluid away from the boundary;
(3) Quadrant III (inward interactions) $u' < 0$, $w' < 0$: a weak inward interaction of fluid toward the boundary (low-speed fluid being pushed back);
(4) Quadrant III (sweep) $u' > 0$, $w' < 0$: a sweep of high-speed fluid toward the boundary.

The results in quadrants II and IV represent a positive downward momentum flux and are involved in turbulent near-bed bursting [29].

In order to describe the turbulence event accurately, the hole (instead of zero) concept is used to eliminate smaller Reynolds stresses. The hole is formed by four hyperbolas $|u'(t)w'(t)| = G_0|u'w'|$, where G_0 is a threshold value. By using the threshold, small values can be ignored in the i-th quadrant [32]. The contribution of each quadrant can be represented by S_k (k = I, II, III, IV, indicating the four quadrants):

$$S_k = \begin{cases} 1, & |u'(t)w'(t)| > G_0\left|\overline{u'w'}\right|_s \\ 0, & otherwise \end{cases} \tag{8}$$

where "" denotes the time average and the subscript s represents steady conditions. In Equation (8), $u'w'$ in steady conditions is introduced to assess the effect of the unsteady flow on turbulent bursting events. The total number of $u'w'$ within a certain time span is set as S, and the occurrence frequency f_s of turbulent bursting events is expressed as follows:

$$f_s = S_k/S \tag{9}$$

Additionally, in the study, the threshold G_0 was set to 1.0 [33], which means that the absolute Reynolds stresses were counted once the stresses were larger than the average Reynolds stresses, a most intuitive choice for the G_0 value. Then, the revised occurrence frequency, f_k, for the four turbulent events is given as follows:

$$f_k = \frac{\sum_{t=0}^{T} S_k}{\sum_{t=0}^{T} S_I + \sum_{t=0}^{T} S_{II} + \sum_{t=0}^{T} S_{III} + \sum_{t=0}^{T} S_{IV}} \tag{10}$$

where T is the length of a certain time span. Figure 9 presents the occurrence frequency f_s of turbulent bursting events for Cases UQ1D1 and UQ2D1. In Figure 9, the x-axis represents the different stages of unsteady flow conditions, "steady" represents the time before the time-varying water depth occurs (see Figure 2), and "t" and "T_d", respectively, denote the starting time of the unsteady flow events and the timespan from the water depth of the steady flows to the peak water depth, i.e., $\frac{t}{T_d} = 1$ denotes the time when the water depth reaches its peak. Figure 9 shows that the turbulent bursting events peak in the falling stage

($\frac{t}{T_d} = 1.5$) for Case UQ1D1, but for Case UQ2D1, the peak appears right after the peak of the water depth, similar to the trend of the TKE results. The results suggest that the turbulent energy dissipation during the unsteady flow period is likely due to the elevated bursting events.

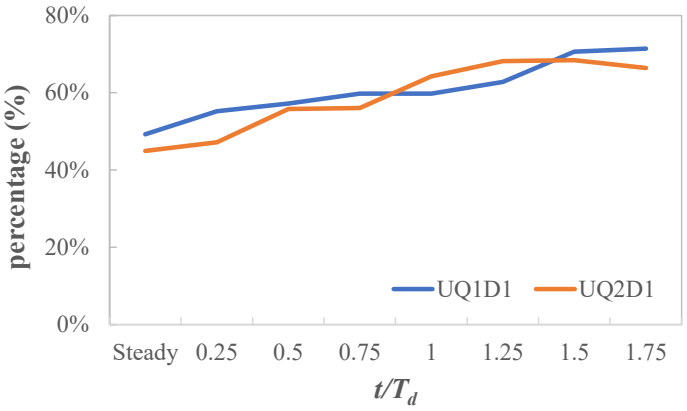
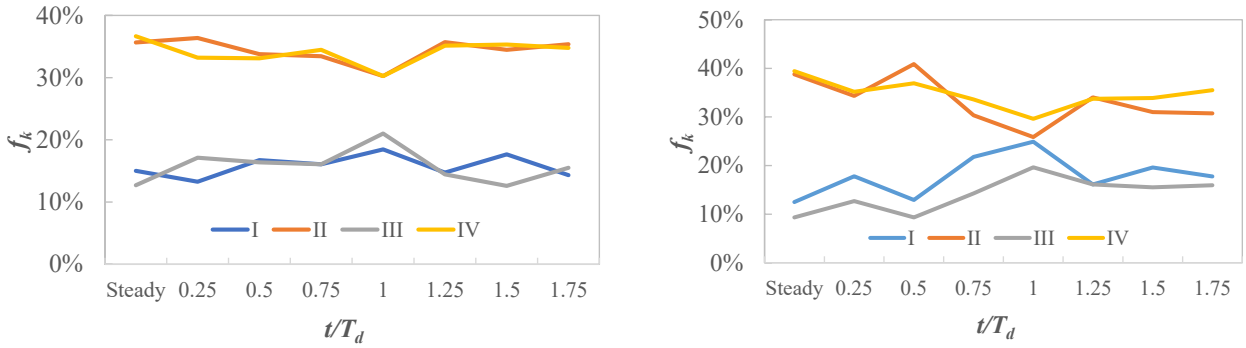


Figure 9. Percentage of occurrence of turbulent bursting events for Cases UQ1D1 and UQ2D1.

Figure 10 shows the frequency of occurrence of coherence turbulent events for Cases UQ1U1 and UQ2D1. It can be observed that sweeps and ejections (quadrants II and IV) occur with comparable frequency, which is much higher than the occurrence frequency of outward and inward interactions. The results indicate that the upward motion of the low-speed fluid (sweep) and the downward motion of the high-speed fluid (ejection) are dominant, similar to the results found in a straight open channel [26,34]. When the water depth reaches its peak ($\frac{t}{T_sd} = 1$), the frequency of occurrence of the outward interaction (quadrant I) and inward interaction (quadrant III) increases due to flow unsteadiness, possibly suggesting the strong interaction of the turbulent structures with the main flow.



(**a**) (**b**)

Figure 10. Frequency of occurrence of coherence turbulent events at different times for Cases UQ1D1 and UQ2D1. (**a**) Case UQ1D1; (**b**) Case UQ2D1.

In order to demonstrate the importance of turbulent bursting (especially the extreme events) to the momentum fluxes, the contributions of large $u'w'$ events to total momentum fluxes in different cases are shown in Figure 11, which adopted the top 30%, 20%, and 10% values as the large amplitude bursting events for statistical analysis [35]. The extreme events in momentum exchange are increased because of flow unsteadiness. The top 30%, 20%, and 10% values reach the maximum at $\frac{t}{T_d} = 1.25$ after the peak of the water depth. The results reveal the crucial role of extreme events in momentum exchange during the unsteady flow period.

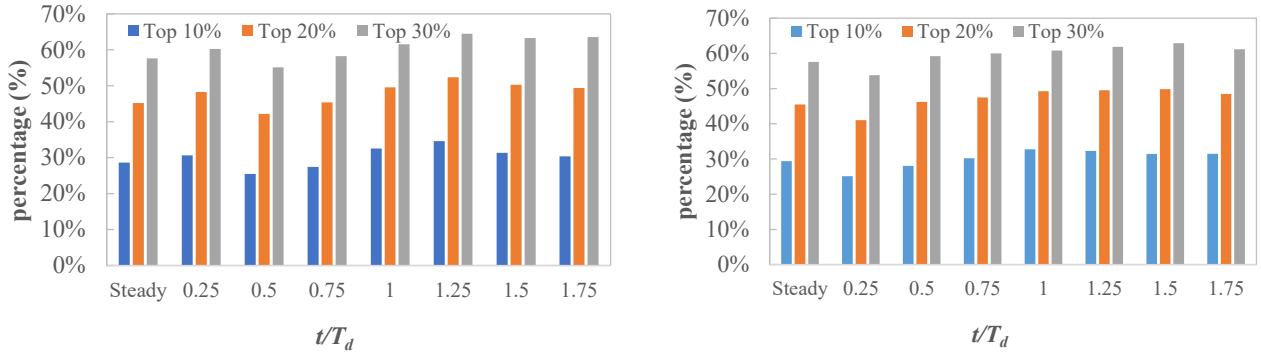


Figure 11. Contributions of large $u'w'$ events to total momentum at different times. (**a**) Case UQ1D1; (**b**) Case UQ2D1.

3.1.4. Power Spectral Density Analysis

Figure 12 shows the PSD S_{xx} of the streamwise fluctuation velocities measured using a 25 Hz ADV, with a different frequency f for the steady, rising, and falling stages of the different cases. For cases near the bed (Figure 12a,b), the attenuation rate k of the PSD in the high-frequency part of the steady stage is close to $-5/3$, as obtained by Kolmogorov scaling [29]. During the rising and falling stages, the attenuation rate k of the PSD in the high-frequency part no long follows the $-5/3$ law, and the energy contained in the high-frequency part for both the rising and falling stages is more than that in the steady stage. For Case UQ1D1, when the frequency f is larger than 0.7 Hz, the PSD curve in the falling stage is greater than that in the rising stage, which means the turbulent energy is greater in the falling stage than that in the rising stage, which is consistent with the *TKE* results. On the other hand, for Case UQ2D1, the turbulent energy during the rising and falling stages is approximately the same, but it is larger than that in the steady stage, which is also similar to the TKE results. Based on the results in Figure 12a,b, it seems that the turbulent energy increases in the rising and falling stages are due to the generation of small-scale turbulence vortices or eddies. For the cases away from the bed (Cases UQ1D2 and UQ2D2), the PSD is smaller than that for Cases UQ1D1 and UQ2D2, which represents less turbulent energy. It also shows that the turbulent energy during the rising and falling stages is only slightly larger than that in the steady stage, and the part with larger energy that concentrates in the high-frequency part means more small-scale turbulence vortices or eddies are generated.

3.2. Cases with a Submerged Vane

This section reports and discusses the experimental results of unsteady flows with a submerged vane.

3.2.1. Time-Varying Water Depth and Streamwise Velocity

Figure 13 demonstrates the time-varying average streamwise velocity behind a submerged vane; Case UQ2D2 is provided for comparison. It can be seen that, due to the presence of a submerged vane, the peaks of the streamwise velocity and water depth occur at approximately the same time. The presence of the vane reduces the streamwise flow velocity in comparison with the bare bed case. In terms of the angle of attack β, for Figure 13a, i.e., $x/L_v = 0.3$, the peak streamwise velocity for $\beta = 0^0$ is the largest among the three β values (0°, 10°, and 20°). As the β values increase, the streamwise velocity first decreases and then increases, representing the complicated features of the induced vortex. For $x/L_v = 4$, the streamwise velocity of $\beta = 10^0$ increases and is comparable with the streamwise velocity at $x/L_v = 0.3$. On the other hand, the streamwise velocity of $\beta = 20^0$ (Case UQ2D2SA20X4) at $x/L_v = 4$ significantly decreases, suggesting the decay of the

induced vortex. It can also be noted that during the falling stage, the streamwise velocity at $x/L_v = 4$ rapidly decreases, which is possibly due to the incoming flow interacting with the reflected flow from the channel outlet.

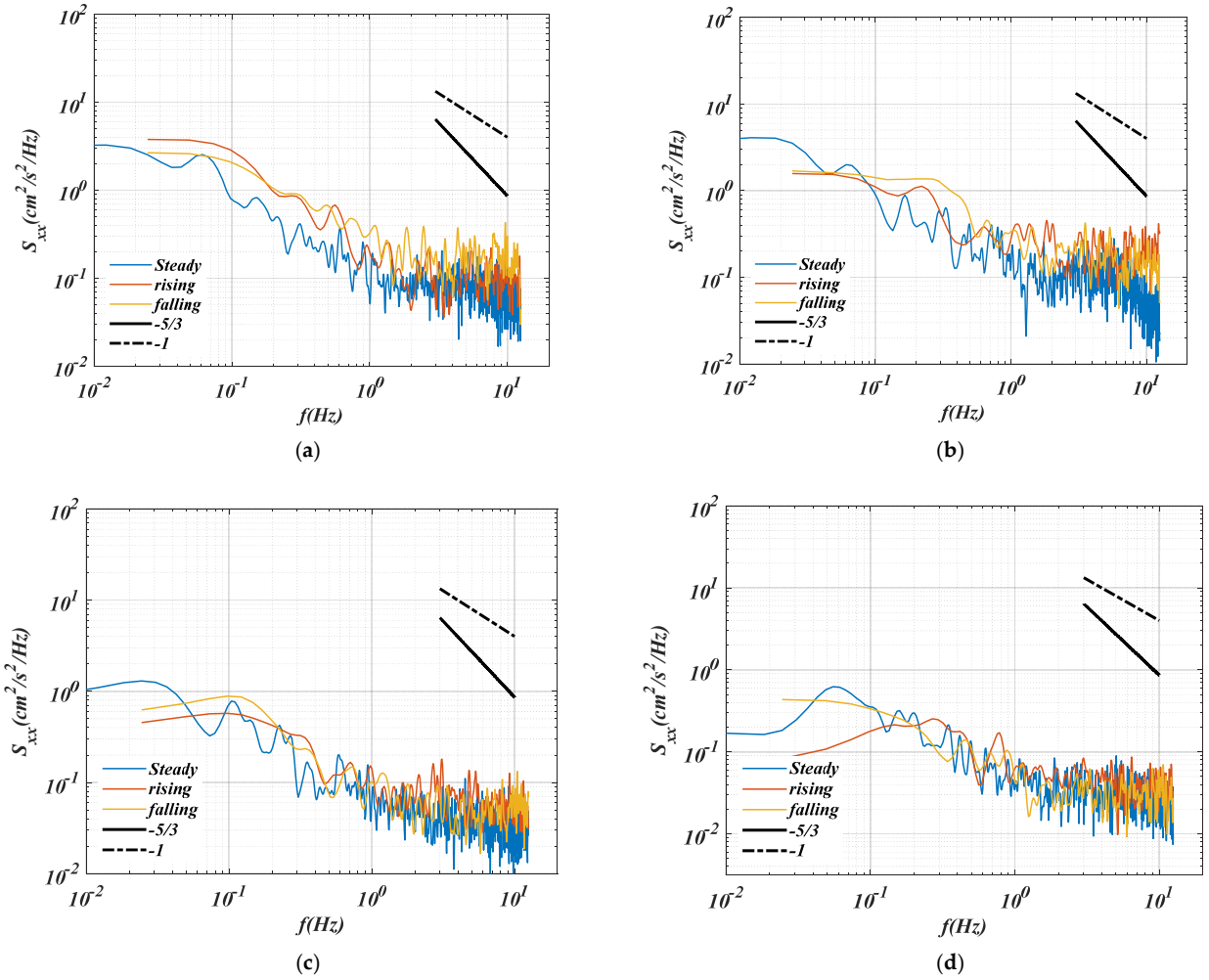


Figure 12. PSD of steady, rising, and falling stages for bare bed cases. (**a**) UQ1D1; (**b**) UQ2D1; (**c**) UQ1D2; (**d**) UQ2D2.

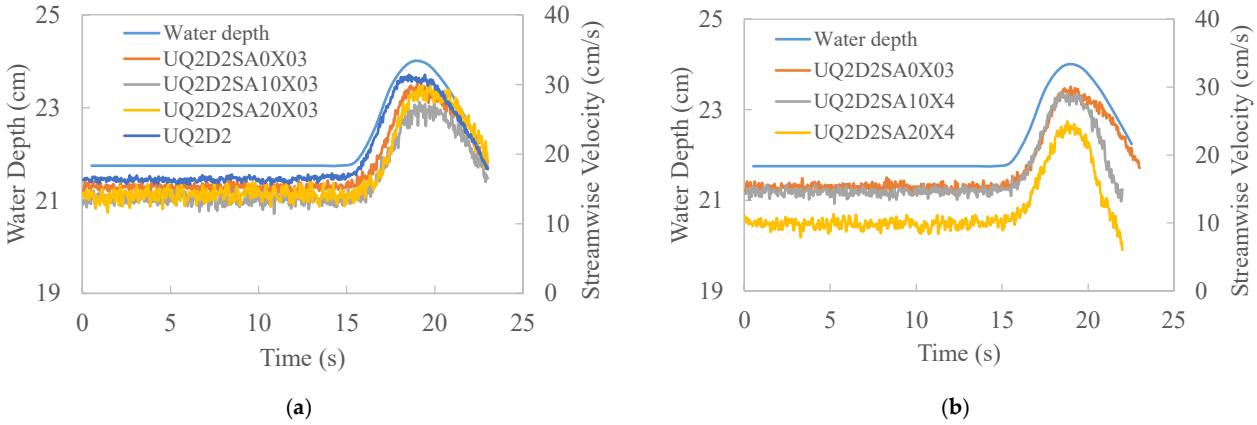


Figure 13. Time-varying water depth and averaged streamwise velocity for the cases with a submerged vane at different locations. (**a**) $x/L_v = 0.3$; (**b**)$x/L_v = 4$.

3.2.2. Time-Varying Turbulent Intensity and Turbulence Kinetic Energy

Figure 14 provides the time-varying turbulent intensity behind a submerged vane. The results reveal that in comparison with the counterpart bare bed cases (UQ2D2, same measurement depth), the turbulent intensities u_{rms}, v_{rms}, and w_{rms} are greater for the cases with a submerged vane. In addition, the ratios u_{rms}, $/v_{rms}$ and u_{rms}, $/w_{rms}$ with the submerged cases are larger than the bare bed case, indicating that the induced vortex elevates the turbulent intensity along the cross section. As the angle of attack β increases, the turbulent intensities u_{rms}, v_{rms}, and w_{rms} increase as well, which means that the induced vortex becomes stronger and the wake region is larger [16,35]. For the Case SQ1 series with $\beta = 20^{\circ}$ at $x/L_v = 0.3$, the turbulent intensities u_{rms}, v_{rms}, and w_{rms} considerably increase during the falling stage. These situations occur for the Case UQ2 series with $\beta = 10^{\circ}$ and 20° at $x/L_v = 4$, possibly owing to the breaking up of the induced vortex that released a substantial amount of turbulent energy.

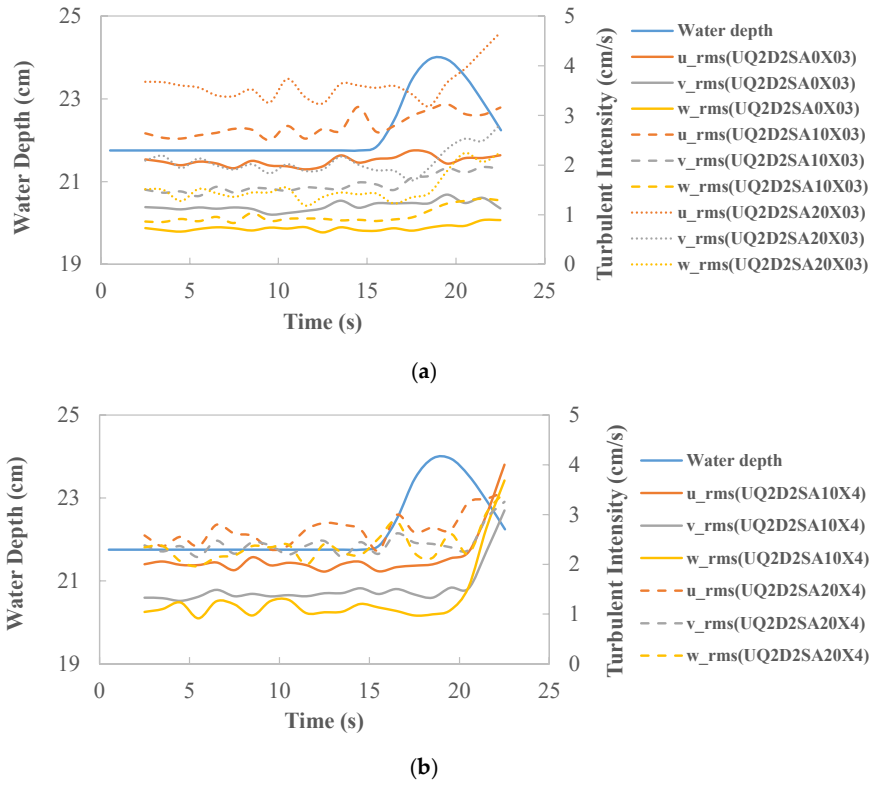


Figure 14. Time-varying turbulent intensities u_{rms}, v_{rms}, and w_{rms} against water depth at different locations. (**a**) Case UQ2 series (with a submerged vane) at $x/L_v = 0.3$; (**b**) Case UQ2 series (with a submerged vane) at $x/L_v = 4$.

The time-varying TKE is presented in Figure 15, where the TKE is normalized by the maximum TKE. In Figure 15a, the TKE of Case UQ2D2SA20X03 abruptly improves in the falling stages, implying the possible break-up of the induced vortex, but the TKE of Cases UQ2D2SA0X03 and UQ2D2SA10X03 does not show this trend. In Figure 15b, i.e., $x/L_v = 4$, the TKEs of Cases UQ2D2SA10X4 and UQ2D2SA20X4 both become notably larger during the falling stage. For Case UQ2D2SA20X4, the sudden increases of the TKE may be due to the passage of the breaking vortex from the upstream. Similarly, for Case UQ2D2SA10X4, the sharp increase in the TKE is also because of the vortex breaking, but it occurs further downstream as compared to Case UQ2D2SA20X4. In addition, the maximum TKE for Case UQ2D2SA10X4 is larger than that for Case UQ2D2SA20X4, suggesting that the vortex breaking of Case UQ2D2SA20X4 occurs earlier than that of Case UQ2D2SA10X4. Furthermore, the TKE of Case UQ2D2SA20X4 decays faster than that of Case UQ2D2SA10X4 due to the mutual interaction of vortices as well as the viscosity of the flow [35].

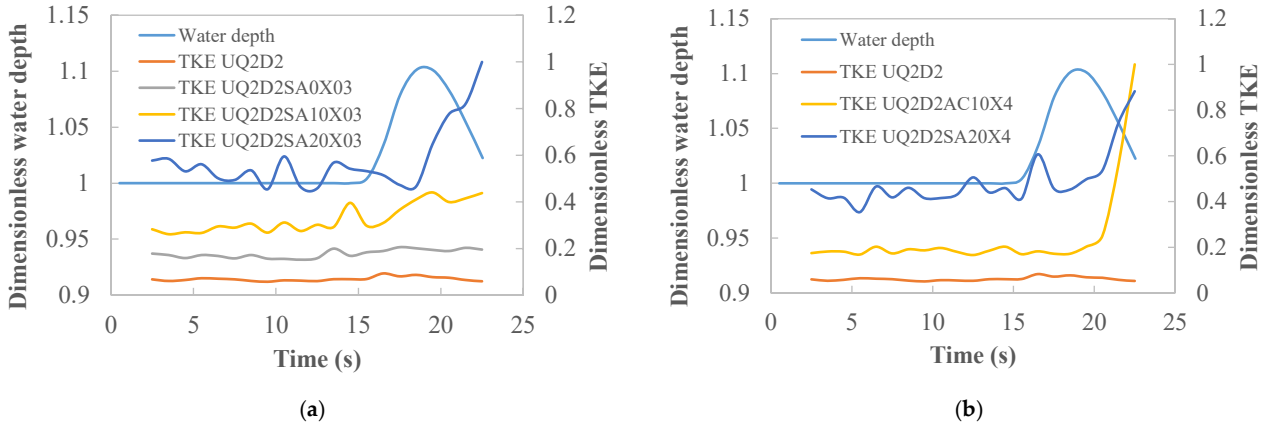


Figure 15. Time-varying dimensionless TKE against dimensionless water depth for the Case UQ2 series at different locations. (**a**) Case UQ2 series (with a submerged vane) at x/L_v = 0.3; (**b**) Case UQ2 series (with a submerged vane) at x/L_v = 4.

3.2.3. Power Spectral Density Analysis

Figure 16 shows the PSD of the streamwise fluctuation velocity for different cases with a submerged vane. In Figure 16a–c, i.e., x/L_v = 0.3, the results show that the turbulent energy during the rising and falling stages is larger in the high-frequency part (small-scale turbulence vortices or eddies) than that in the steady stage, similar to the results found in the bare bed case. It can also be seen that the PSD of cases with a larger angle of attack β is greater, which indicates that the submerged vane with a larger β can induce more turbulent energy along the streamwise direction. Additionally, the turbulent energy for cases with a larger β value declines faster in the high-frequency part. Therefore, the presence of a submerged vane can produce more small-scale turbulence vortices or eddies but leads to the more rapid decay of turbulent energy during unsteady flow events. Figure 16d,e provides the PSD for the areas further downstream (x/L_v = 4) of a submerged vane. It can be seen that turbulent energy decreases more at locations further downstream and with a faster attenuation rate. Furthermore, the turbulent energy during the falling stage is obviously greater than that during the rising and steady stages.

Figure 17 presents the PSD *Syy* of the transverse fluctuation velocity for different cases of a submerged vane. In Figure 17a, similar to Figure 16a, the turbulent energy during the rising and falling stages is larger in the high-frequency part (small-scale turbulence vortices or eddies) than that during the steady stage. Furthermore, there are multiple spikes (dashed circle in Figure 17a) in the high-frequency part, possibly denoting the shedding frequency from the induced vortex. Regarding Figure 17b, there are some obvious spikes (colored arrows in Figure 17b) during the steady, rising, and falling stages. For the steady stage, the spike that could be the shedding frequency f of the induced vortex is at 2 Hz. Using the mean streamwise velocity u_m = 0.16 m/s and the characteristic length (length of the submerged vane) L_v = 0.32 m yields a Strouhal number St ($= \frac{fL_v}{u_m}$) of 1 in the steady stage. For the rising and falling stages of Case SQ2C10X03, by using the average streamwise velocity, i.e., u_m = 0.25 m/s, the St values during the rising and falling stages are approximately 1.92 and 5.12, respectively. For Case SQ2C20X03 ($\beta = 20°$, x/L_v = 0.3), the peak frequencies (colored arrows in Figure 17b) as well as the St values decrease. In Figure 17b,d, i.e., further downstream (x/L_v = 4), peak frequencies become unobvious, possibly because the induced vortex decayed or due to other factors such as the mixing of the turbulence generated from the free surface or channel bed with the turbulence from the induced vortex. Similar to the PSD *Syy* of the streamwise fluctuation velocity, the PSD *Syy* of the transverse fluctuation velocity at x/L_v = 4 performs rapidly and attenuates in the high-frequency part.

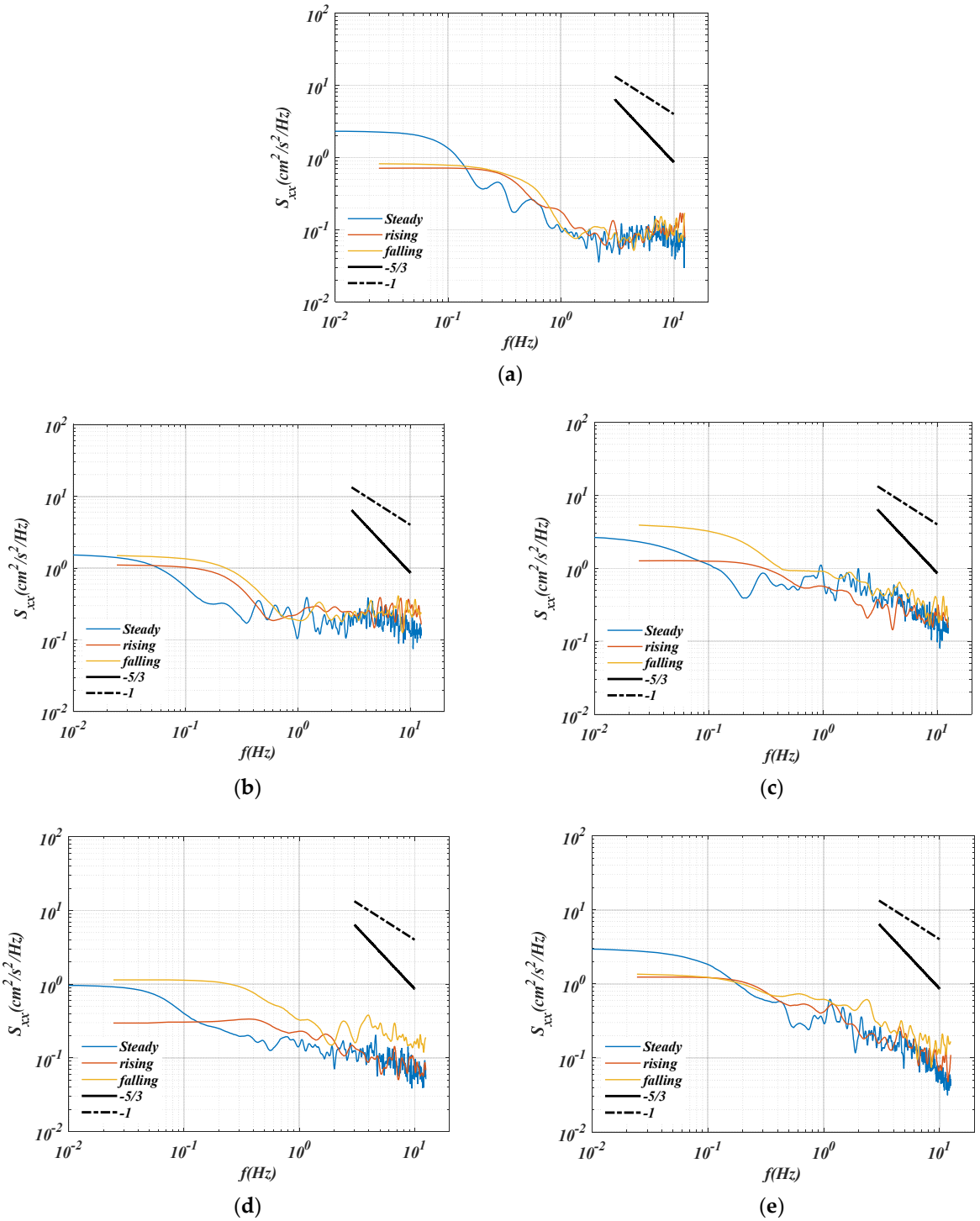


Figure 16. PSD *Sxx* of steady, rising, and falling stages with a submerged vane. (**a**) UQ2D2SA0X03; (**b**) UQ2D2SA10X03; (**c**) UQ2D2SA20X03; (**d**) UQ2D2SA10X4; (**e**) UQ2D2SA20X4.

The above analysis is based on the comparison of the bare bed case and the presence of a submerged vane at a height h_m of 9.08 cm from the bed. For other depths, such as $h_m = 0.43$ cm and $h_m = 11.58$ cm, the two locations are close to the bed and water surface, respectively. Therefore, the vane-induced vortex shedding would have less effects only on the unsteady flow field instead of the case with $h_m = 9.08$ cm. This conjecture needs to be verified in the future.

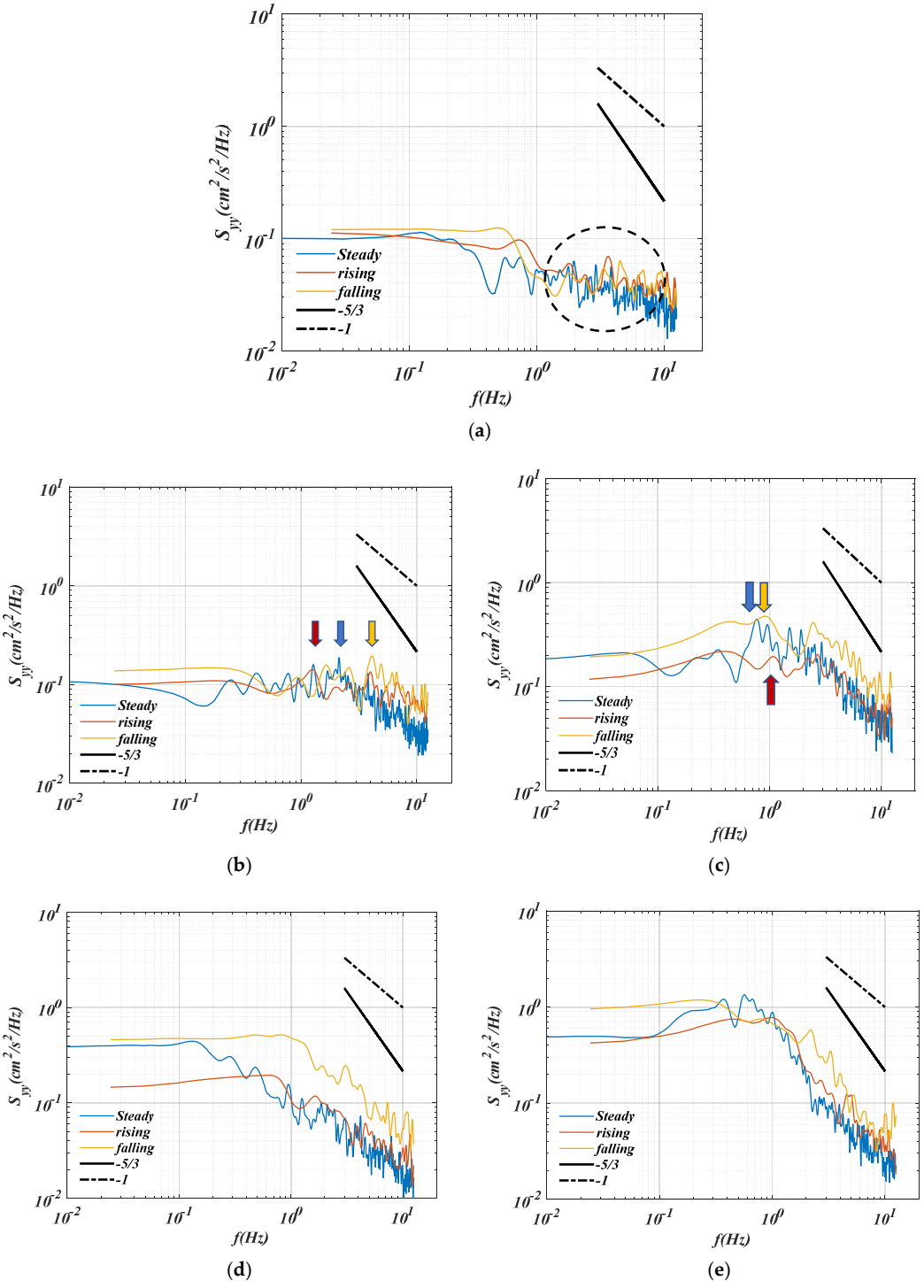


Figure 17. PSD *Syy* of steady, rising, and falling stages with a submerged vane (Note: the dashed circle in (**a**) represents regions with multiple spikes, and the colored arrows in (**b**,**c**) denote the local spikes). (**a**) UQ2D2SA0X03; (**b**) UQ2D2SA10X03; (**c**) UQ2D2SA20X03; (**d**) UQ2D2SA10X4; (**e**) UQ2D2SA20X4.

4. Conclusions

In this study, repeated flume experiments under the same unsteady flow conditions were carried out, and the ADV was used to obtain the instantaneous three-dimensional velocity. The ensemble average method was adopted to obtain the time-varying average velocity, and the Reynolds decomposition was in turn used to disintegrate the instanta-

neous velocity into time-varying average velocity and fluctuating velocity. Turbulence characteristics such as turbulent intensity, turbulent bursting, and power spectral density were analyzed against water depth variations. Several conclusions can be drawn, which are summarized below:

(1) Based on variations of the TKE, the ensemble average method using 20 repeated measurements was adopted to obtain meaningful turbulence information.
(2) For bare bed conditions, two cases (Case UQ1 and UQ2 series), each with a different unsteadiness parameter α and loop pattern, were studied. The results show that the loop pattern of streamwise velocity against the water depth variations could significantly affect the turbulence characteristics of unsteady flow.
(3) Over a bare bed, for the case with the several-crossing loop pattern (Case UQ1 series), the peak of the streamwise velocity occurred approximately at the peak of the water depth, and the difference between the streamwise velocity near the bed and away from the bed kept increasing during the rising and falling stages of the unsteady flow. For the case with a classic "eight-shape loop" pattern (Case UQ2 series), the streamwise velocity reached its peak earlier than the water depth, and the differences between the streamwise velocity changes near the bed and away from the bed followed the trend of the water depth, with the difference being larger during the falling stage than that during the rising stage.
(4) Over a bare bed, the turbulent intensity and TKE were larger near the bottom and became smaller when the measurement location was further away from the bottom. In addition, near the bed, the peaks of the turbulent intensity and TKE lagged behind the peak of the water depth. The PSD revealed that the increases in turbulent energy during the rising and falling stages were due to the generation of small-scale turbulence vortices or eddies. The results also implied that the bottom roughness is an important factor in delaying the peak of the turbulence quantities during unsteady flow periods. When the water depth reached its peak, the frequency of occurrence of the outward interaction (quadrant I) and inward interaction (quadrant III) increased due to flow unsteadiness, suggesting the possible strong interaction of the turbulent structures with the main flow.
(5) With a submerged vane, as the values of the angle of attack β increased, the streamwise velocity first decreased and then increased, representing the complicated features of the induced vortex. The increase in β values caused the increase in the turbulent intensity and TKE, which means that the induced vortex became stronger and the wake region was larger. When β was equal to 20°, the TKE abruptly increased in the falling stages, implying the possible break-up of the induced vortex.
(6) With a submerged vane, the PSD of the streamwise fluctuation velocity *Sxx* revealed that turbulent energy during the rising and falling stages was larger in the high-frequency part (small-scale turbulence vortices or eddies) than that in the steady stage, similar to the results found for the bare bed case. The PSD *Syy* of the transverse fluctuation velocity showed multiple spikes in the high-frequency part, possibly denoting the shedding frequency from the induced vortex. Further downstream, the peak frequencies of the PSD *Syy* became unobvious because of the decay of the induced vortex or other factors such as the mixing of the turbulence generated from the free surface or channel bed with the turbulence from the induced vortex.

Due to climate change, strong unsteady flows, such as flash flooding, are becoming more frequent and could cause significant loss of human life and property. Based on the findings in the study, some potential sustainable solutions in hydraulic engineering can be proposed to protect our society in the future. For example, since bottom roughness could delay the peak of turbulence quantities during unsteady flow periods, placing coarse particles over the channel bed is possibly helpful and can prevent the peak flow from interacting with the peak turbulence quantities. Once the peak of the turbulence quantities appears in the falling stage of an unsteady flow, the materials eroded by strong, turbulent motions at the bottom of a river will be carried away by a smaller flow velocity

and transported a shorter distance, which can alleviate the damage caused by a strong unsteady flow to hydraulic structures. In addition, because flash flooding events could significantly amplify turbulence quantities and bed shear, hydraulic structures need to be reinforced with high standards to mitigate the bed erosion caused by flash flooding events. These aspects should be considered in the sustainable design of future hydraulic engineering projects.

In this study, because the ensemble average method was adopted, due to time constraints and logistic effort, the measurement points and repeated times were very limited. In the future, more repeated measurements in the laboratory will be required to be able to provide more detailed turbulence characteristics for different locations and planes over a bare bed and with a submerged vane. It would be of interest to test the ensemble average method using repeated measurements higher than 20 for the cases with a submerged vane. The experimental results in the paper can also be combined with numerical simulations to shed more light on unsteady flow dynamics.

Author Contributions: Conceptualization, Y.-T.L. and S.J.; methodology, K.H., Y.-T.L., and T.H.; laboratory measurement, Y.-T.L.; data analysis, S.J. and J.H.; software, T.H. and K.H.; writing—original draft preparation, K.H. and Y.-T.L.; writing—review and editing, J.H. and S.J.; funding acquisition, Y.-T.L., X.Y., and K.H. All authors have read and agreed to the published version of the manuscript.

Funding: This research was funded by the Science and Technology Plan Project of Zhejiang Provincial Department of Water Resources (Grant No. RA2010), the Science Foundation of Donghai Laboratory (Grant No. DH-2022KF01016), and the Zhejiang Provincial Natural Science Foundation of China (Grant no. LY20A020009).

Institutional Review Board Statement: Not applicable.

Informed Consent Statement: Not applicable.

Data Availability Statement: All data, models, or codes that support the findings of this study are available from the corresponding author upon reasonable request.

Acknowledgments: The author Y.-T.L. is grateful to the deceased John A. Hoopes in Civil and Environmental Engineering, University of Wisconsin–Madison for his guidance and help in designing, studying, and analyzing the unsteady flow experiments and the associated datasets.

Conflicts of Interest: The authors declare no conflict of interest.

References

1. Gaume, E.; Bain, V.; Bernardara, P.; Newinger, O.; Barbuc, M.; Bateman, A.; Blaškovičová, L.; Blöschl, G.; Borga, M.; Dumitrescu, A.; et al. A compilation of data on european flash floods. *J. Hydrol.* **2009**, *367*, 70–78. [CrossRef]
2. Westra, S.; Fowler, H.J.; Evans, J.P.; Alexander, L.V.; Berg, P.; Johnson, F.; Kendon, E.J.; Lenderink, G.; Roberts, N. Future changes to the intensity and frequency of short-duration extreme rainfall. *Rev. Geophys.* **2015**, *52*, 522–555. [CrossRef]
3. Todeschini, S. Trends in long daily rainfall series of Lombardia (Northern Italy) affecting urban stormwater control. *Int. J. Climatol.* **2012**, *32*, 900–919. [CrossRef]
4. Tamm, O.; Saaremae, E.; Rahkema, K.; Jaagus, J.; Tamm, T. The intensification of short-duration rainfall extremes due to climate change—Need for a frequent update of intensity–duration–frequency curves. *Clim. Serv.* **2023**, *30*, 100349. [CrossRef]
5. Kuhnle, R.A. Bed load transport during rising and falling stages on two small streams. *Earth Surf. Process. Landf.* **1992**, *17*, 191–197. [CrossRef]
6. Lee, K.T.; Liu, Y.L.; Cheng, K.H. Experimental investigation of bedload transport processes under unsteady flow conditions. *Hydrol. Process.* **2004**, *18*, 2439–2454. [CrossRef]
7. Nezu, I.; Kadota, A.; Nakagawa, H. Turbulent structure in unsteady depth-varying open-channel flows. *J. Hydraul. Eng.* **1997**, *123*, 752–763. [CrossRef]
8. Song, T.; Graf, W.H. Velocity and turbulence distribution in unsteady open-channel flows. *J. Hydraul. Eng.* **1996**, *122*, 141–154. [CrossRef]
9. Hopkinson, L.C.; Walburn, C.Z. Near-boundary velocity and turbulence in depth-varying stream flows. *Environ. Fluid Mech.* **2016**, *16*, 559–574. [CrossRef]
10. Bombar, G. Hysterisis and shear velocity in unsteady flows. *J. Appl. Fluid Mech.* **2016**, *9*, 839–853. [CrossRef]

11. Aleixo, R.; Soares-Frazão, S.; Zech, Y. Statistical analysis methods for transient flows—The dambreak case. *J. Hydraul. Res.* **2020**, *57*, 688–702. [CrossRef]
12. Huang, N.E.; Shen, Z.; Long, S.R.; Wu, M.C.; Shih, H.H.; Zheng, Q.; Yen, N.C.; Tung, C.C.; Liu, H.H. The empirical mode decomposition and the Hilbert spectrum for nonlinear and non-stationary time series analysis. *Proc. R. Soc. A Math. Phys. Eng. Sci.* **1998**, *454*, 903–995. [CrossRef]
13. Huang, N.E.; Wu, Z. A review on Hilbert-Huang transform: Method and its applications to geophysical studies. *Rev. Geophys.* **2008**, *46*, RG2006. [CrossRef]
14. Bradshaw, P. *An Introduction to Turbulence and Its Measurement*; Thermodynamics and Fluid Mechanics Series; Pergamon Press: Oxford, UK, 1971.
15. Chanson, H. Statistical analysis methods for transient flows—The dam-break case. *J. Hydraul. Res.* **2020**, *58*, 1001–1004. [CrossRef]
16. Erdog, E.; Yagci, O.; Kirca, V.S.O. Hysterical effects in flow structure behind a finite array of cylinders under gradually varying unsteady flow conditions. *J. Ocean Eng. Mar. Energy* **2022**, *8*, 247–267. [CrossRef]
17. Xu, Y.L.; Chen, J. Characterizing nonstationary wind speed using empirical mode decomposition. *J. Struct. Eng.* **2004**, *130*, 912–920. [CrossRef]
18. Odgaard, A.J.; Wang, Y. Sediment management with submerged vanes. II: Applications. *J. Hydraul. Eng.* **1991**, *117*, 284–302. [CrossRef]
19. Sharma, H.; Ahmad, Z. Enhancing transverse mixing in streams with submerged vanes. *Environ. Fluid Mech.* **2018**, *18*, 661–681. [CrossRef]
20. Lee, B.O.; Fitzpatrick, F.A.; Hoopes, J.A. Effectiveness of submerged vanes for stabilizing streamside bluffs. *J. Hydraul. Eng.* **2021**, *147*, 04020093. [CrossRef]
21. Ouyang, H.T.; Lai, J.S.; Yu, H.; Lu, C.H. Interaction between submerged vanes for sediment management. *J. Hydraul. Res.* **2008**, *46*, 620–627. [CrossRef]
22. Odgaard, A.J. *River Training and Sediment Management with Submerged Vanes*; ASCE: Reston, VA, USA, 2009.
23. SonTek. *Acoustic Doppler Velocimeter (ADV) Operation Manual (Firmware Version 4.0)*; SonTek: San Diego, CA, USA, 1997; 115p.
24. Nezu, I. Open-Channel flow turbulence and its Research Prospect in the 21st Century. *J. Hydraul. Eng.* **2004**, *131*, 229–246. [CrossRef]
25. Chang, K.-A.; Liu, P.L.-F. Experimental investigation of turbulence generated by breaking waves in water of intermediate depth. *Phys. Fluids* **1999**, *11*, 3390–3400. [CrossRef]
26. Yang, Y.; Lin, Y.T.; Ji, X. Hydrodynamic characteristics of flow over emergent vegetation in a strongly curved channel. *J. Hydraul. Res.* **2021**, *60*, 240–257. [CrossRef]
27. Huang, T.; He, M.; Hong, K.; Lin, Y.; Jiao, P. Effect of Rigid Vegetation Arrangement on the Mixed Layer of Curved Channel Flow. *J. Mar. Sci. Eng.* **2023**, *11*, 213. [CrossRef]
28. Kim, S.C.; Friedrichs, C.T.; Maa, J.Y.; Wright, L.D. Estimating bottom stress in tidal boundary layer from Acoustic Doppler Velocimeter data. *J. Hydraul. Eng.* **2000**, *126*, 399–406. [CrossRef]
29. Han, D.R.; Guo, Y.; Jiao, P.; Yuan, Y.; Lin, Y.T.; He, Z.G. Coherent structures, turbulence intermittency, and anisotropy of gravity currents propagating on a rough and porous bed. *Phys. Fluids* **2023**, *35*, 016611. [CrossRef]
30. Mazumder, B.S.; Pal, D.K.; Ghoshal, K.; Ojha, S.P. Turbulence statistics of flow over isolated scalene and isosceles triangular-shaped bedforms. *J. Hydraul. Res.* **2009**, *47*, 626–637. [CrossRef]
31. Kassem, H.; Thompson, C.E.L.; Amos, C.L.; Townend, I.H. Wave-induced coherent turbulence structures and sediment resuspension in the nearshore of a prototype-scale sandy barrier beach. *Cont. Shelf Res.* **2015**, *109*, 78–94. [CrossRef]
32. Lu, S.S.; Willmarth, W.W. Measurements of the structure of the Reynolds stress in a turbulent boundary layer. *J. Fluid Mech.* **1973**, *60*, 481–511. [CrossRef]
33. Lin, Y.-T.; Yang, Y.; Chiu, Y.-J.; Ji, X. Hydrodynamic Characteristics of Flow in a Strongly Curved Channel with Gravel Beds. *Water* **2021**, *13*, 1519. [CrossRef]
34. Yager, E.M.; Schmeeckle, M.W. The influence of vegetation on turbulence and bed load transport. *J. Geophys. Res. Earth. Surf.* **2013**, *118*, 1585–1601. [CrossRef]
35. Sharma, H.; Ahmad, Z. Turbulence characteristics of flow past submerged vanes. *Int. J. Sediment Res.* **2020**, *35*, 42–56. [CrossRef]

Disclaimer/Publisher's Note: The statements, opinions and data contained in all publications are solely those of the individual author(s) and contributor(s) and not of MDPI and/or the editor(s). MDPI and/or the editor(s) disclaim responsibility for any injury to people or property resulting from any ideas, methods, instructions or products referred to in the content.